Electronic Supplementary Material (ESI) for Energy & Environmental Science.

Electronic and nuclear contributions to time-resolved optical and X-ray absorption spectra of hematite and insights into photoelectrochemical performance

Dugan Hayes,*[a] Ryan G. Hadt,[a] Jonathan D. Emery,[b] Amy A. Cordones,[e] Alex B. F. Martinson,[b] Megan L. Shelby,[ad] Kelly A. Fransted,[a] Peter D. Dahlberg,[af] Jiyun Hong,[ad] Xiaoyi Zhang,[c] Qingyu Kong,[c] Robert W. Schoenlein,[e] and Lin X. Chen*[ad]

[a]Chemical Sciences and Engineering Division, [b]Materials Science Division, and [c]X-ray Science Division, Argonne National Laboratory, Argonne, IL 60439, USA. E-mail: hayesd@anl.gov, lchen@anl.gov

[d]Department of Chemistry, Northwestern University, Evanston, IL 60208, USA

[e]Chemical Sciences Division, Lawrence Berkeley National Laboratory, Berkeley, CA 94709, USA

[f]Graduate Program in the Biophysical Sciences, The James Franck Institute, and The Institute for Biophysical Dynamics, The University of Chicago, Chicago, IL 60637, USA

Electronic Supplementary Information

1. Sample preparation

Atomic layer deposition (ALD) of both Fe_2O_3 and Al_2O_3 was performed using a Cambridge Nanotech Inc. Savannah 200 ALD reactor. Fused-quartz (FQ) substrates (Solaronix SA) were first sonicated for 10 minutes eacj in acetone and then isopropyl alcohol. Between sonications substrates were rinsed with water and blown dry with N_2. Both FQ substrates and Si_3N_4 windows (Norcada) were loaded into the 200 °C chamber and allowed to sit for 1 hr at temperature prior to deposition. FQ samples were set directly on the reactor surface, while Si_3N_4 were mounted such that precursor exposure was equal on both sides of the window. All substrates were ozone-cleaned immediately prior to Fe_2O_3 deposition.

Fe_2O_3 ALD parameters was selected based on the work of Martinson *et al.*[1] Dose-purge sequences of t_1-t_2-t_3-t_4 were employed (times reported in seconds), where t_1 and t_3 were ferrocene (Fe(Cp2)$_{2,}$ 98%, Aldrich, held at 150 °C) and ozone (5% O_3 in high-purity O_2¸ supplied with a DelOzone corona arc discharge generator) dose times, respectively, and t_2 and t_4 were purge times. The $Fe(Cp)_2$ t_1 dose was delivered in a pair of 2 second sub-doses followed by a 28 second soak under quasi-static exposure (vacuum pump lines closed). 400 cycles of dose sequence (t_1)-t_2-t_3-t_4 = (2[28]-2[28])-20-90-30 were run, yielding ~20 nm thick amorphous as-grown Fe_2O_3 films. These amorphous films were converted to hematite via a 1.5-hr, 500 °C anneal in high-purity, flowing (200 sccm) O_2. To passivate the Fe_2O_3/FQ surface defects,[2] 20 cycles of trimethylaluminum(TMA, 97%, Aldrich,)-H_2O was deposited on some post-annealed samples. Dose-purge times were t_1-t_2-t_3-t_4 = 0.015-10-0.015-10. This sequence deposited ~2 nm of amorphous Al_2O_3 on the Fe_2O_3.

A sample of bulk hematite was prepared for transient absorption measurements by grinding 50 mg dry hematite powder (Sigma Aldrich) with a mortar and pestle, adding two drops of Fluorolube (Gabriel Performance Products), and grinding again to give a mull. A portion of the mull was spread thinly onto a sapphire window, and the sample position for OTA measurements was chosen to optimize the amplitude and signal to noise of the transient signal.

The aqueous sample of $[Fe(H_2O)_6]^{3+}$ was prepared by dissolving reagent grade iron(III) chloride (Sigma Aldrich) in Milli-Q water and diluting to achieve an optical density of 0.55 at 415 nm in a 2 mm path length quartz cuvette. The sample was stirred throughout the OTA measurements. The drop cast film of $[Fe(H_2O)_6]^{3+}$ was prepared from the same aqueous solution of iron(III) chloride. A drop of the solution was place on a bare fused quartz substrate and air dried under ambient conditions.

2. Data analysis and fitting

All data analysis was performed using MATLAB R2013a (MathWorks). All fits were obtained using the nonlinear least-squares fitting function lsqcurvefit. Although lower and upper bounds were used to constrain some of the fits to physical parameter spaces, all fits converged to solutions in which the variables were not approaching their respective bounds.

3. Steady state optical absorption and reflectance

Steady state optical absorption spectra were measured using a Beckman Coulter DU 800 spectrophotometer, and reflectance spectra were measured using a Varian Cary 5000 with integrating sphere accessory (DRA-2500). The blank used for these measurements was the same fused quartz used as the substrate for preparing the ALD hematite samples. The 700-800 nm region of the reflectance spectrum was fit to the same region of the absorption spectrum using a scaling factor and a constant offset as fit parameters, and the reflectance-corrected absorption spectrum was taken as the absorption spectrum minus the scaled reflectance spectrum. These spectra are shown in Fig. S1.

The reflectance-corrected optical absorption spectrum was fit in the region from 222 to 800 nm to the sum of seven Gaussian bands as described in the main text. This fit is shown in Fig. 1 and the fit parameters are given in Table S1.

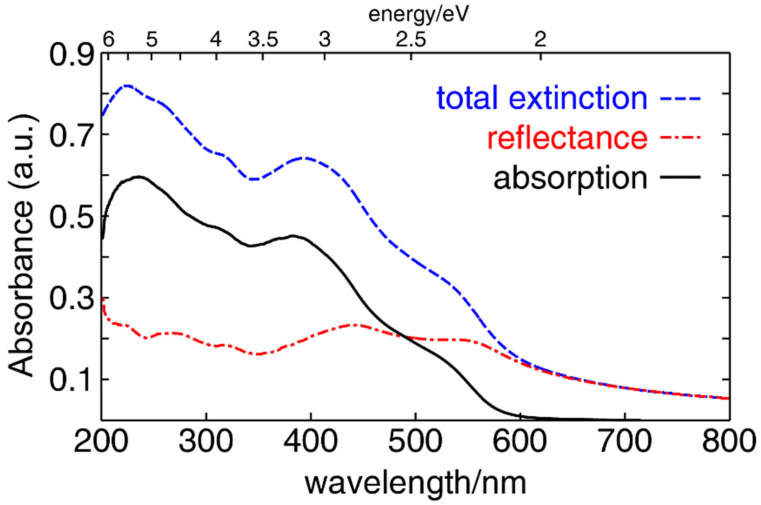

Fig. S1. The raw absorption spectrum obtained for a 20 nm hematite thin film on fused quartz without reflectance correction (dashed blue), the reflectance spectrum obtained from an integrating sphere measurement (dot-dashed red), and the corresponding reflectance-corrected absorption spectrum used throughout the main text (solid black).

Table S1.

	Peak area (a.u.)	Frequency (eV)	Linewidth (FWHM, eV)
LMCT 1	1.000	5.32	2.40
LMCT 2	0.231	3.22	0.91
d-d 1	0.009	2.31	0.21
d-d 2	0.017	2.48	0.30
d-d 3	0.029	2.80	0.51
d-d 4	0.041	3.90	0.55
d-d 5	0.058	4.30	0.85

4. Visible and NIR transient absorption

Ultrafast transient absorption measurements were performed using a commercial regeneratively amplified Ti:Sapphire laser (Spectra-Physics) and an automated data acquisition system (Ultrafast Systems, Helios). A 1.0 kHz pulse train of 100 fs, 2.9 mJ pulses centered at 830 nm was produced by a Spitfire Pro amplifier seeded by a Mai Tai oscillator and pumped by an Empower frequency-doubled, diode-pumped Nd:YLF Q-switched laser. One third of the total power was used for the transient absorption experiments. The beam was split, with 90% of the beam used for the pump and 10% used for the probe. The pump was focused into a Type 1 second harmonic generation (SHG) BBO crystal, and the 415 nm component was isolated using a dichroic filter. The pump beam was then passed through a depolarizer, attenuated to the desired power using an absorptive neutral density filter, and chopped at

500 Hz. The probe beam was delayed relative to the pump with a retroreflector mounted on a motorized delay stage and focused into a sapphire plate to generate a white light continuum. For the visible probe experiments, the beam was passed through a high pass filter to give a continuum spanning from 430 to 750 nm, while for the NIR probe experiments, the beam was passed through a low pass filter to give a continuum spanning from 900 to 1500 nm. For UV-vis probe experiments, the probe beam was instead focused into a translating CaF_2 plate and passed through a high pass filter to give a continuum spanning from 315 to 750 nm. The pump and probe beams were focused and overlapped at the sample position with beam radii ($1/e^2$) of 130 and 85 µm, respectively, and the transmitted probe was focused into a fiber-coupled multichannel spectrometer and CMOS sensor. Unless otherwise stated, all OTA measurements were performed with a pump pulse energy of 4.6 µJ (17 mJ/cm^2 fluence).

For some experiments, the first or third harmonics of the pump beam were used instead of the second harmonic. For the first harmonic, the pump beam was used directly. For the third harmonic, the beam waist was reduced to 3 mm and tripled using the following sequence of optics: 1) a 415 nm half waveplate, 2) a Type 1 SHG BBO crystal, 3) a dual-wavelength (415 and 830 nm) half waveplate, 4) a calcite group velocity dispersion compensation plate, 5) a Type 1 THG BBO crystal, and 6) a dichroic mirror reflective at 277 nm. All optical components for THG were purchased from Eksma Optics. For experiments conducted using excitations wavelengths that are not harmonics of the Ti:Sapph fundamental, the desired wavelength was obtained using a home-built two-stage optical parametric amplifier (OPA), which has been described previously.[3] Briefly, ~1% of the beam was focused into a sapphire plate to generate a white light continuum, which was used to seed parametric amplification in the first BBO. The output of the first stage was then used to seed the second stage. The 415 nm beam was split into two paths to pump both amplification stages, and the output beam was isolated from the pump beams by a dichroic mirror transmissive at 415 nm. Fig. S2 shows a comparison of TA results obtained using excitations wavelengths from the second harmonic and the OPA and UV-vis, visible, and NIR white light continuum probes.

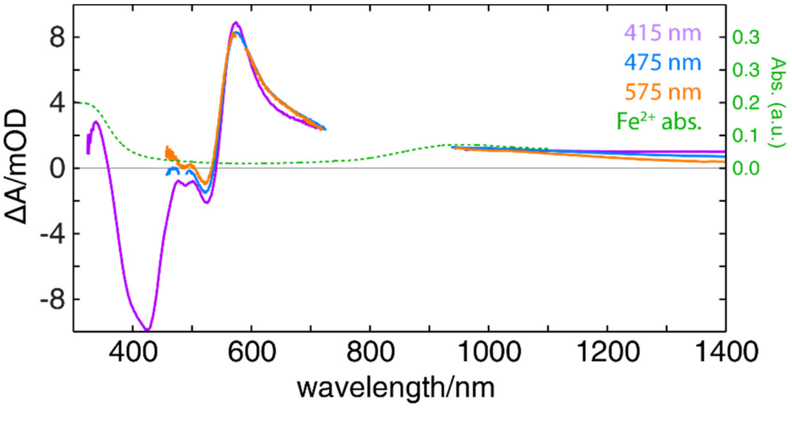

Fig. S2. The OTA spectra of hematite extending from the visible into the NIR at a 20 ps delay time are plotted for three different excitation wavelengths. The probe region between 730 and 930 nm is inaccessible due to proximity to the 830 nm fundamental from which the white light continua are generated. The visible white light continuum used for the 475 and 575 nm spectra (blue and orange, respectively) was generated by focusing the 830 nm beam into a static sapphire plate, while the visible-NUV continuum used for the 415 nm spectrum (lavender) was generated by focusing into a rotating CaF_2 plate. The absorption spectrum of Fe2+ (dotted green) is also shown for comparison in the NIR.

Specular reflectance-corrected OTA measurements were obtained by rotating the sample 30° in the direction of the incident beam, blocking the transmitted probe beam, and redirecting the specular probe beam into the spectrometer. Transmission measurements at the same time delays were performed immediately after to ensure pump power, spot size, overlap, and incidence angle were the same. The probe-only and pump-and-probe spectra were recorded separately so the reflected probe spectra could be added to the transmission spectra before the ΔOD spectra were calculated, as shown in Equation S1.

$$\Delta OD(\omega) = -\log\left(\frac{PP_t(\omega) + cPP_r(\omega)}{P_t(\omega) + cP_R(\omega)}\right) \tag{S1}$$

Here, $PP(\omega)$ and $P(\omega)$ correspond to the pump-and-probe and pump-only spectra, respectively, with subscripts indicating the measurement mode of the spectrum (i.e. transmission or reflection), and c is a multiplicative constant. We employ this constant to take into account for the possibility that the reflected beam may not be focused as efficiently into the fiber optic of the detector as the transmitted beam. Fig. S3 shows reflectance-corrected TA spectra for several values of c, including the purely reflective ($c = \infty$) and transmissive ($c = 0$) limits.

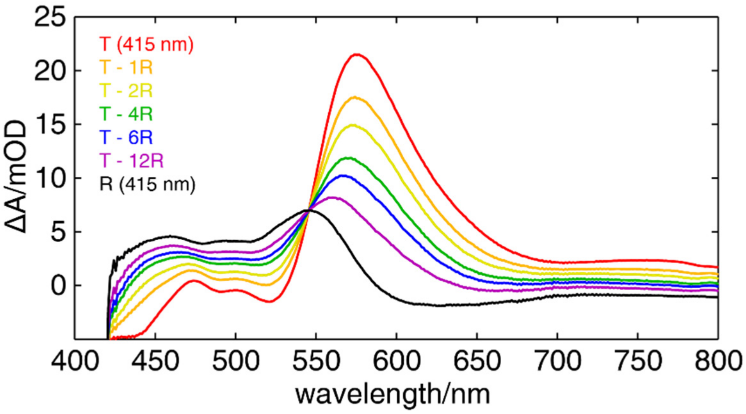

Fig. S3. The optical transient absorption spectrum measured at a delay time of 20 ps with a pump wavelength of 415 nm (red) and the optical transient specular reflectivity spectrum measured for the same conditions (black). The reflectance-corrected OTA spectrum is calculated by adding the specular reflections to the pump+probe and probe spectra before taking the negative logarithm of the ratio of the two (orange). Because the measurements are performed separately with different optical paths, the reflectance is scaled by increasing amounts from 2-12x when performing this calculation, and these traces are shown in yellow, green, blue, and purple.

By following the evolution of the spectral shape between the two limits, it is clear that, qualitatively, the OTA spectrum is only significantly impacted for high values of c (i.e. ≥ 4). The actual value of c is most likely only slightly greater than 1, so we conclude that reflectance correction of the OTA spectrum is not necessary to model the main features. Furthermore, we choose not to perform reflectance correction in the OTA spectra reported in the main text because of two additional complications beyond uncertainty in the value of c. First, the reflectance spectrum is strongly dependent on incidence angle, and uncertainly in this value for different pump and probe beams (i.e. first, second, and third harmonics; OPA; UV-vis, visible, and NIR continua) would make direct comparison of spectra collected under different conditions difficult. Instead, all experiments were performed in a near-normal incidence geometry, with the pump and probe approaching the sample at ±5° relative to the normal. Second, the variable-temperature UV-vis measurements to which the OTA measurements are compared were performed with an instrument incapable of measuring the reflectance spectrum. Because temperature-dependent changes in reflectance are necessarily present in the variable-temperature spectra, it is appropriate to keep the laser-induced changes in reflectance in the OTA spectra.

Kinetic traces were fit to the model given by Equation S2, where *n* is the number of decay components included in the fit and the time constant of the *n*th component is taken to be infinite. The first *n* terms correspond to the analytical solution of a Gaussian instrument response function (IRF) with root variance τ_0 centered at $t = t_0$ convolved with an exponential decay with a time constant of τ_i. The first term corresponds to the *n*th component with $\tau_n = \infty$ and gives a constant offset at times $t \gg \tau_0$. The final term accounts for the coherent artifact at $t = \tau_0$, which is modeled as a Gaussian with root variance τ_c. The amplitudes A_i and time constants τ_i were taken as variables in the least-squares fits along with the time zero t_0, IRF width τ_0, and coherent artifact parameters A_c and τ_c, giving a total of *n*+3 variables. For long-time OTA measurements (see Section S11), a coherent artifact was not observed, so the final term of equation S2 was not included to obtain the fit shown in Fig. 10.

$$\begin{aligned}\Delta OD(t) = {} & A_n\left(1-\operatorname{erf}\left(\frac{-(t-t_0)}{\sqrt{2}\tau_0}\right)\right) \\ & + \sum_{i=1}^{n-1} A_i \exp\left(\frac{\tau_0^2}{2\tau_i^2}-\frac{t-t_0}{\tau_i}\right)\left(1-\operatorname{erf}\left(\frac{\tau_0^2-\tau_i(t-t_0)}{\sqrt{2}\tau_0\tau_i}\right)\right) \\ & + A_c\exp\left(\frac{-(t-t_0)^2}{2\tau_c^2}\right)\end{aligned} \tag{S2}$$

5. Variable temperature measurements

Steady state optical and hard X-ray absorption measurements were performed on a hematite thin film sample that was affixed to a copper heating element with silver epoxy (MG Chemicals). The sample was heated using a Model 336 Cryogenic Temperature Controller (LakeShore Cryotronics). For both measurements, the sample was aligned such that the beam passed 5 mm below the copper heating element and the temperature was cycled three times between 300 and 500 K in steps of 100 K, with absorption spectra measured for each temperature point in each cycle.

For the optical experiment, the thermal difference spectrum was fit according to Equation 1 as described in the main text and shown in Fig. 3. The values of the fit parameters are given below in Table S2. These values are expressed relative to those obtained from the fit to the steady state spectrum, which are given in Table S1.

Table S2.

	Amplitude change (%)	**Frequency shift (cm^{-1})**	**Linewidth change (%)**
LMCT 1	2.0	-390	2.2
LMCT 2	-0.3	-570	3.9
d-d 1	52	190	33
d-d 2	-44	400	-8.5
d-d 3	-70	-70	-19
d-d 4	94	230	35
d-d 5	-77	1700	-35

To determine if an individual laser pulse deposits enough energy into the hematite sample to raise the temperature enough to account for the strong OTA signal, we carefully measured the laser fluence at the sample under conditions that reproduce the magnitude of the thermal difference spectrum at 575 nm. The thermal difference spectrum exhibits a ΔOD of 3.25 mOD at 575 nm, as shown in Fig. 2 of the main text. To obtain an OTA spectrum with the same 3.25 mOD magnitude at 575 nm, a pump energy of 1.82 µJ/pulse was required for a pump wavelength of 415 nm and a Gaussian beam radius of 130 µm. From these values, and assuming a Gaussian beam profile, we calculate the pump fluence to be:

$$\frac{2 * 1.82\ \mu\mathrm{J}}{\pi * (130\ \mu\mathrm{m})^2} = 7.0\ \frac{\mathrm{mJ}}{\mathrm{cm}^2}. \tag{S3}$$

However, we note that the spot size of the probe beam is significantly smaller than the spot size of the pump beam (to ensure nearly uniform sample excitation), and thus the pump fluence should instead be calculated for this smaller area at the center of the Gaussian beam profile. Measurement of the probe spot size must also take into account the spatial chirp in the probe beam inherent to the generation of the white light continuum (that is, the probe spot size at a particular wavelength or wavelength range is smaller than the total probe spot size). The probe beam radius at 575 nm was measured to be 34 µm by using a razor blade to cut the total counts measured at 575 nm on the CCD camera. Using this value, we can calculate the percentage of the laser power contained in the small area at the center of the Gaussian beam profile that overlaps with the 575 nm probe. By taking the ratio of the integrals of the 2D beam profiles over the relevant distances (34 µm/130 µm = 0.26), we obtain:

$$\%\ \text{power} = \frac{\int_{-0.26\sigma}^{0.26\sigma}\int_{-0.26\sigma}^{0.26\sigma} A * \exp\left(-2\left(\frac{x^2}{\sigma^2}+\frac{y^2}{\sigma^2}\right)\right)dxdy}{\int_{-\sigma}^{\sigma}\int_{-\sigma}^{\sigma} A * \exp\left(-2\left(\frac{x^2}{\sigma^2}+\frac{y^2}{\sigma^2}\right)\right)dxdy} * 100\% = 17.5\%. \tag{S4}$$

Therefore, we may recalculate the pump fluence at the probe spot size using a pulse energy of $0.175 * 1.82\ \mu\mathrm{J} = 0.318\ \mu\mathrm{J}$. Although there will be some variation in fluence across the probe spot size, the average fluence may be obtained using a flat-top beam profile to give:

$$\frac{0.318\ \mu\mathrm{J}}{\pi * (34\ \mu\mathrm{m})^2} = 8.76\ \frac{\mathrm{mJ}}{\mathrm{cm}^2}. \tag{S5}$$

The light harvesting efficiency at 415 nm was measured to be 0.37 (see Fig. 11), and thus, a total of 3.21 mJ/cm^2 is absorbed by the sample from each laser pulse. Using a density of 5.26 g/cm^3,[4] a heat capacity of 0.65 J/g·K,[5] and a film thickness of 20 nm, the temperature change of the film resulting from the absorption of this amount of energy is calculated as follows:

$$3.21 \times 10^{-3}\ \frac{\mathrm{J}}{\mathrm{cm}^2} * \frac{\mathrm{g}\cdot\mathrm{K}}{0.65\ \mathrm{J}} * \frac{\mathrm{cm}^3}{5.26\ \mathrm{g}} * \frac{1}{20 \times 10^{-7}\mathrm{cm}} = 469\ \mathrm{K}. \tag{S6}$$

Thus, we find that the maximum temperature increase from this pump fluence is ~470 K. Some of the laser energy will be dissipated by non-thermal (e.g. photochemical) pathways, and some thermal energy is also expected to be transferred into the quartz substrate. These factors likely account for the difference between the calculated maximum temperature increase and the 200 K temperature increase used in the steady state measurement to obtain the same signal magnitude. Overall, we find that the laser deposits more than enough energy into the sample than is required to account for the temperature increase used to obtain the steady state difference spectrum, and we conclude that our thermal model is fully consistent with a simple equilibrium consideration of the temperature of the film upon laser excitation.

6. Variable fluence transient absorption

Variable fluence OTA measurements were performed using a continuously variable neutral density wheel in the pump beam path immediately following the depolarizer. The pump power was measured at the sample. The results are shown in Fig. S4, where each spectrum is normalized to its maximum value.

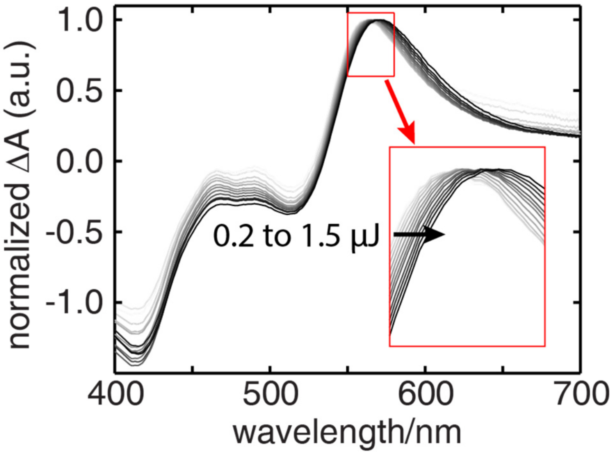

Fig. S4. The normalized OTA spectra of hematite as pulse energy is increased from 0.2 to 1.5 μJ (0.75-5.7 mJ/cm^2 fluence). A zoom of the enclosed part of the spectrum shows the peak shift further toward the red end of the spectrum as pulse energy increases.

7. DFT calculations

All density functional theory (DFT) and time-dependent DFT (TD-DFT) calculations were carried out using Gaussian 09, revision A.02,[6] software installed on the Blues or Fusion clusters at Argonne National Laboratory. All calculations were carried out using the B3LYP functional[7,8] (spin unrestricted, high-spin Fe(III)), in combination with a triple-ζ TZVP basis set[9] on all atoms. Geometries for TD-DFT calculations (75 states) were based on the optimized octahedral geometry calculated for $[Fe(H_2O)_6]^{3+}$, in which all Fe-O bond distances were 2.06 Å. For room temperature hematite, the oxygen atoms of the water ligands were moved ±0.08 Å from the octahedral geometry, with three long bonds and three short bonds in the C_{3v} (*fac*) orientation, to match the geometry taken from X-ray crystallographic data.[10] For high temperature hematite, the oxygen atoms were similarly moved +0.090 and -0.076 Å from the octahedral geometry to match the thermal lattice expansion observed in X-ray powder diffraction data.[11] For both distorted geometries, all Fe and O atoms were frozen and the positions of the hydrogens were subsequently optimized. To simulate absorption and transient absorption difference spectra, TD-DFT calculated sticks with corresponding oscillator strengths were broadened with Gaussian functions with full-width half maxima of 1.0 and 2.0 eV for out-of-plane and in-plane LMCT transitions, respectively. The in-plane LMCT band was also shifted 2.17 eV lower in energy to match the experimental absorption spectrum of hematite. These spectra are shown in Fig. S5.

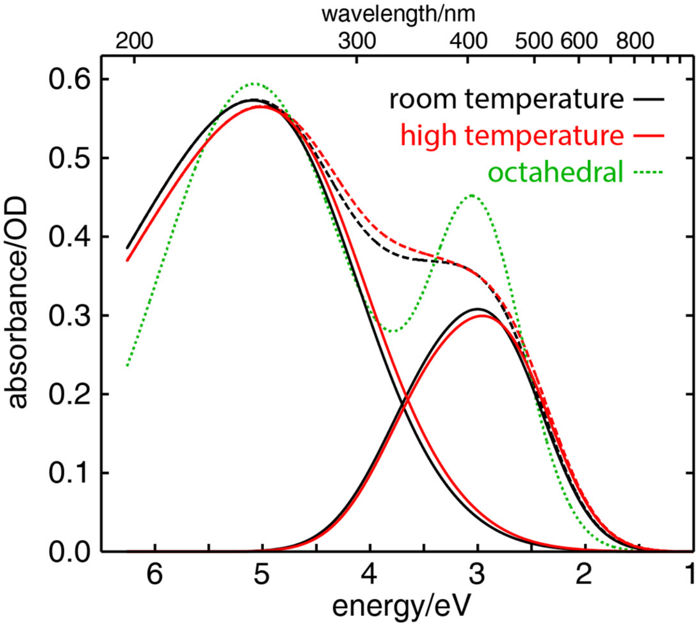

Fig. S5. DFT calculations on a single $[Fe(H_2O)_6]^{3+}$ complex with Fe-O bonds lengths distorted to match the geometry of bulk hematite at room temperature (black) and high temperature (red). The individual bands are shown (solid curves) along with the total spectra (dashed lines). The spectrum was also calculated in the same manner for the optimized octahedral geometry of $[Fe(H_2O)_6]^{3+}$ and shown for comparison (dotted green).

8. Oxygen K-edge transient absorption

Oxygen K-edge measurements were performed at beamline 6.0.2 of the Advanced Light Source (Lawrence Berkeley National Laboratory). The undulator-based soft X-ray beamline is equipped with an X-ray chopper (run at 4 kHz), varied line-space grating monochromator, and amplified Ti:Sapphire laser system (run at 2 kHz).[12,13] A multi-bunch operation mode was used in which 275 electron bunches are filled with 2 ns bunch spacing and a single “camshaft” bunch is separated by a 100 ns filling gap. Custom electronics synchronized the laser pulse to a single “camshaft” bunch from alternating chopper openings (interleaving pumped and unpumped spectra). The sample was a 20 nm hematite thin film on a 100 nm Si_3N_4 window (see Section 1 above). X-rays were transmitted through the sample and the synchronized “camshaft” bunch was recorded with gated detection using a fast avalanche photodiode.

Laser excitation was provided at various harmonics of the Ti:Sapphire laser system (400 and 267 nm) or using an optical parametric amplifier (TOPAS-C) at 500 nm. The pulse duration was stretched to approximately 0.5 ps. The laser spot size at the sample position was set to be at least twice as large as the X-ray probe and provided excitation intensities ranging from 0.7-14 mJ/cm^2. Specifically, the fluences used at each excitation wavelength were 1.3 mJ/cm^2 at 267 nm, 1.7 mJ/cm^2 at 400 nm, and 2.0 mJ/cm^2 at 500 nm. The X-ray probe (65x75 µm) was overlapped spatially and temporally with the laser pulse. Temporal resolution was limited by the 70 ps X-ray pulse duration. Energy resolution was 0.5 eV.

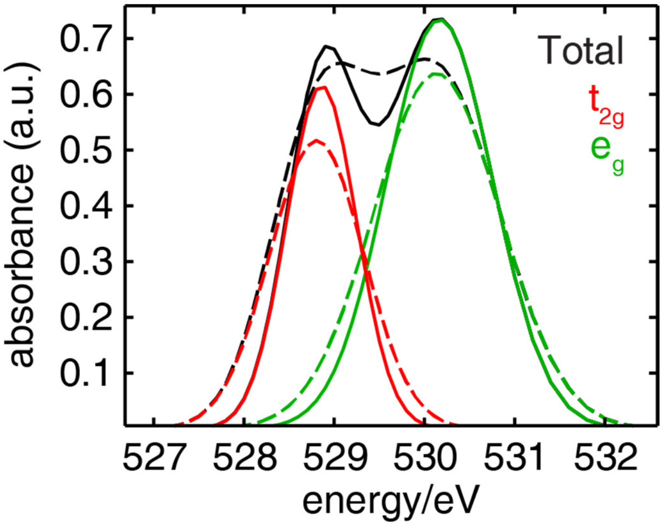

Fig. S6. The individual t_{2g} and e_g components (red and green, respectively) of the fits to the steady state oxygen pre-edge absorption spectrum (solid traces) and the transient absorption spectrum (dashed traces) shown in Fig. 6. The sum of the two components for each fit are shown in black. The fit parameters are collected in Table S3.

Table S3.

Steady state fit component	Peak area (a.u.)	Frequency (eV)	Linewidth (eV)
t2g	1.00	528.86	0.39
eg	1.81	530.17	0.59
Edge	26.8	538.83	2.29

Difference fit component	Peak area change (%)	Frequency shift (cm^{-1})	Linewidth change (%)
t2g	13	-430	34
eg	3.2	-260	19
Edge	41	6000	19

9. Iron K-edge absorption

Transient and steady-state iron K-edge absorption measurements were performed at beamline 11-ID-D at the Advanced Photon Source (APS, Argonne National Laboratory). The experimental details of transient absorption measurements at this beamline have been reported elsewhere,[14–16] but the experiments reported here differ in three significant ways: 1) The APS was operated in hybrid fill mode; 2) The excitation source for some measurements was the second harmonic of a Ti:Sapphire laser; and 3) The sample was a thin film. Each of these differences are detailed below.

1. Hybrid fill operating mode. In this continuous top-up mode, the 102 mA ring current of the APS is divided into a 16 mA singlet bunch followed by a train of 56 smaller bunches with an orbit period of 3.68 µs. The rms bunch length of the 16 mA singlet is 50 ps.

2. Excitation source. For some experiments, the excitation source was the same as that reported previously.[14,15] The 351.926 MHz rf signal from the storage ring was divided by 4 and used to trigger an electronic delay generator (PDL-100A-20NS, Colby Instruments) connected to the mode-lock driver of a diode-pumped Nd:YLF oscillator (Lightwave, LW-131). A timing stabilizer (Time-Bandwidth CLX-1100) was used to phase-lock the oscillator cavity with the rf/4 signal from the storage ring. The oscillator output was used to seed a Q-switched Nd:YLF regenerative amplifier (Quantronix). The 271.5 kHz signal from the storage ring corresponding to the orbit period was used to trigger a digital delay generator (DG535, Stanford Research Systems) that subsequently triggered the Q-switch at a repetition rate of 1.6 kHz. The 1053 nm beam, with a pulse energy of 2.0 mJ and duration of 5 ps (FWHM), was then either doubled with a Type 1 BBO crystal to give a 527 nm beam with 0.80 mJ/pulse or tripled with a series of two Type 1 BBO crystals to give a 351 nm beam with 0.35 mJ/pulse. In either case, the desired harmonic was isolated using an appropriate dichroic mirror.

For other experiments, the excitation source was a commercial renegeratively amplified Ti:Sapphire laser system (Coherent). A 10 kHz pulse train of 100 fs, 1.0 mJ pulses centered at 800 nm was produced by a Legend Elite Duo amplifier seeded by a Micra-5 oscillator and pumped by an Evolution intracavity-doubled, diode-pumped Nd:YLF Q-switched laser. The oscillator was phase locked to the rf/4 signal of the storage ring using the Synchrolock AP system (Coherent), and the Q-switch was triggered as described above for the other laser system. The 800 nm beam was doubled using a Type 1 BBO crystal to give a 400 nm beam with 0.20 mJ/pulse.

In either case, the laser power was adjusted using an absorptive neutral density filter and focused such that the beam is converging at the sample position and reaches the focal point behind the sample. The laser spot size at the sample was 2 mm. The laser and X-ray beams were overlapped at the sample position by aligning through a pinhole. A fast photodiode and 8 GHz oscilloscope (Infinium, Agilent) was then used to set the zero time delay between the singlet X-ray bunch and the laser pulse by adjusting the timing of the mode-lock driver or the Synchrolock.

3. Thin film sample. Most experiments performed at 11-ID-D are conducted using a flowing jet with the sample either in solution or suspension in a solvent. In this case, our sample was a 20 nm thin film of hematite on a 1.5 mm fused quartz substrate, so X-ray fluorescence could only be collected from the front surface. Furthermore, the beam incidence of the laser had to be sufficiently rotated from 45° to ensure the specular reflection was not directed into the detector, which was positioned at 90° relative to the X-ray beam path. Thus, the sample was mounted such that the X-ray beam incidence was 22.5° relative to the normal of the film, and a single avalanche photodiode (APD) detector was used. The sample holder was mounted on a vertical translation stage to permit one-dimensional rastering of the sample between XANES scans.

The X-ray probe pulses were obtained from the storage ring electron bunches using dual inline undulators followed by an actively stabilized dual crystal Si(111) monochromator. The X-ray spot size at the sample was 0.5 mm (horizontal) x 0.2 mm (vertical). An upstream APD detector channel was used for pulse-by-pulse normalization of the fluorescence signal. A manganese Z-1 filter (3 absorption lengths) and soller slit assembly were mounted between the film and the fluorescence detector to minimize background signal from elastic scattering. The signal of both APD channels was recorded at a 1 GHz sampling rate by a fast analyzer card (Agilent), and the data was processed in real time by software written by Dr. Guy Jennings (APS), which performs background subtraction, pulse shape fitting, and signal averaging.

XANES spectra were acquired with 4 second averaging at each energy point at a pump-probe delay time of 100 ps. The sample was vertically rastered by 0.3 mm between each full XANES scan. A total of 81

XANES scans were performed for 351 and 527 nm excitation, and 40 were performed for 400 nm excitation. The laser power was attenuated to ~80% of the ablation threshold measured for each wavelength. The pulse energies were 68 μJ at 351 nm, 57 μJ at 400 nm, and 110 μJ at 527 nm. The 8 orbits of the hybrid mode singlet bunch before the laser pulse were averaged to give the ground state reference XANES spectrum, and the difference spectra shown in Figures 7, S7-8, and S14 are the difference of the raw spectra obtained from the laser-synchronized orbit and the ground state reference. No normalization or background subtraction was performed on the XANES spectra before taking the difference.

We note here that comparing the XTA spectra and the thermal difference spectra presents a challenge. For the optical experiment, the beam incidence was normal to the surface of the hematite film, and thus thermal expansion of the copper heating element did not affect the measurement. However, for the variable temperature X-ray experiment, the beam incidence was 22.5° relative to the normal, and thus thermal expansion resulted in translation of the sample. Sample translation could result in a change in the total fluorescence signal measured at the detectors for two reasons: 1) the X-ray beam interacts with a region of the sample with a different film thickness, and 2) the sample is pushed closer to the photodiode. Consequently, thermal difference spectra cannot be obtained by simply subtracting raw XANES spectra as was done for the XTA experiment.

Two different approaches to solving this problem were explored. In the first, no attempt was made to adjust for sample translation at different temperatures. The 300 K spectrum was subtracted from the 500 K spectrum without performing normalization on the individual spectra. The resulting difference spectrum was then normalized by fitting to a third order polynomial multiplied by the convolution of a Gaussian and a step function and subtracting this background function. In the second approach, the sample was mounted on a horizontal translation stage. At each temperature point, the sample position was adjusted to match the pre-edge background to that of the room temperature spectrum before the XANES spectrum was acquired. The same subtraction and background fitting procedure was performed for these difference spectra as well. Fig. S7 shows a comparison of the spectra obtained from both approaches with the XTA spectrum. Both 500 K difference spectra reproduce the features of the XTA spectrum well, and they do not show significant variation. Because both approaches are acceptable and the spectra effectively interchangeable, we choose to display the data from the first approach due to the simplicity with which it was acquired.

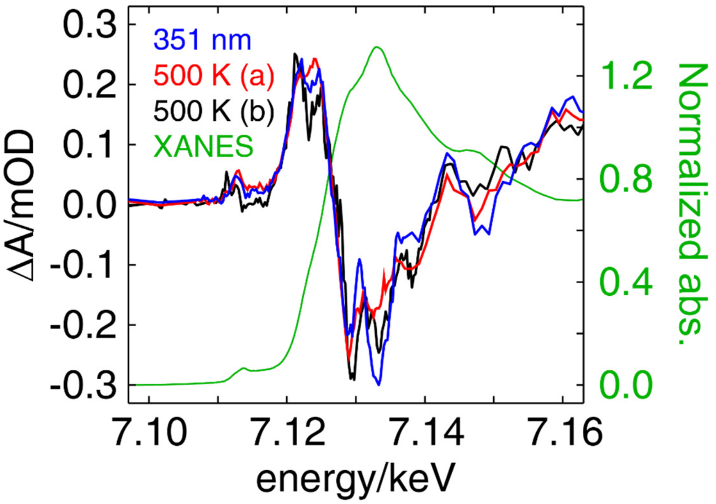

Fig. S7. A comparison of two different methods for acquiring iron K-edge thermal difference spectra (red and black) relative to the XTA spectrum (blue). The steady state XANES spectrum (green) is provided as a reference.

10. FEFF9 full multiple scattering calculations

XANES spectra were calculated using the FEFF9 software package[17,18] using some of the parameters for hematite reported by Katz *et al*.[19] The hematite crystal structure was taken from the cif file published by Finger *et al*.[10], and a cluster with a radius of 20 Å was generated using the ATOMS program[20] within the ARTEMIS software package.[21] The cluster was truncated to all iron atoms within 17.5 Å of the center and all corresponding oxo ligands so every iron atoms was fully hexacoordinated. The cluster had a total of 2470 atoms. The room temperature XANES spectrum for this cluster was calculated using a maximum k value of 5.0, a k step of 0.007, and an amplitude reduction factor of 0.9. The full multiple scattering (FMS) was calculated for a cluster with a radius of 9 Å and self-consistent scattering potentials calculated for a 4.9 Å cluster. Aside from the unique scattering potential given to the central iron atom, all iron atoms were given the same scattering potential, and the same was done for all oxygen atoms. The Hedin-Lundqvist exchange correlation potential was used with a -6.5 eV correction to the Fermi level, and the ground state potential was used for the background function. Both dipole and quadrupole transitions were included in the calculation. The core-hole was screened self-consistently according to the final state rule. The spectrum was thermally broadened using the correlated Debye model with a Debye temperature of 660 K[22] and a temperature of 300 K. XANES spectra were not normalized before calculating difference spectra.

Following the work of Katz *et al*., we first shifted the experimentally measured XANES spectrum by -1.4 eV and subtracted that from the original spectrum to assess the expected features that would arise from transient Fe^{2+} species.[19] This spectrum, shown in Fig. S8a, does not reproduce the strong, well resolved feature at 7.133 keV and in fact shows a stronger negative peak at 7.137 keV. In Fig. S8b, the black spectrum is the difference of the calculated room temperature ground state spectrum (henceforth called the GSS) from the same spectrum shifted by -1.4 eV. Again, this shows poor overall agreement with experiment.

Figs. S8c-d involve the calculation of a next-nearest-neighbor configurationally averaged spectrum for a lattice distortion corresponding to a nearest-neighbor electron small polaron. As demonstrated by Sanson *et al*., EXAFS spectra of iron impurities in $LiNbO_3$ crystals, which have nearly the same C_{3v} geometry as bulk hematite, show nearly symmetric elongation of all Fe-O bonds by ~4% in going from a ferric to a ferrous site.[23] Accordingly, we adopted a simple first-shell model for the polaronic distortion in which the six nearest-neighbor oxygens surrounding a single iron site move isotropically outward. The bond distances of the six oxygen ligands of the central iron atom were increased by 4%, and all other atoms were kept in the same positions. The nearest-neighbor oxygen atoms can be separated into two groups, each of which are three-fold degenerate. The thirteen next-nearest-neighbor shell of iron atoms surrounding the distorted iron can be grouped into five groups, all of which are three-fold degenerate except one that is singly degenerate. A different scattering potential was assigned to each of the different groups of oxygen and iron atoms. Another potential was then assigned to all iron atoms beyond the next-nearest-neighbor shell, and the same was done for all similarly distant oxygen atoms. The XANES spectrum was calculated for the central iron atom and one of each of the five groups of next-nearest-neighbor iron atoms, and the polaronic spectrum was taken to be the weighted average of the six spectra.

The difference of the polaronic spectrum and the GSS is shown in Fig. S8c. In Fig. S8d, the spectrum of the central iron site was also shifted by -1.4 eV before the weighted average was taken and the GSS subtracted to approximate the Fe^{2+} oxidation state of the electron small polaron. While the unshifted polaron model does give a strong negative peak at 7.133 keV and shows reasonable agreement with the data, the shifted polaron model does not. The polaronic deformation should only occur upon formation of a ferrous site, and thus the shifted spectrum should be more representative of the transient spectrum expected for such a species. Adelstein *et al.* have shown that the electron density of a polaron in hematite is almost entirely localized on a single iron site,[24] so this shift should provide a good approximation of the spectrum. Even if the shift is distributed across all 14 irons within the next-nearest-neighbor shell (a shift of -0.1 eV for each iron), the calculated spectrum does not resemble the data. The poor overall agreement between the shifted spectra (Figs. S8a-b and S8d) and the experimental data thus suggests that the contribution of Fe^{2+} species, and thus electron small polarons, to the observed difference spectrum is not significant.

In Figs. S8e-f, thermal disorder was added to the cluster by setting the temperature to 1000 K, while in Fig. S8f, a constant 0.6 eV broadening was also included for both the 1000 K and ground state spectra to account for final state broadening and the energy resolution of the experiment. Both reproduce all features of the experimental spectrum and show good qualitative agreement overall.

For Figs. S8g-h, the hematite clusters were generated from cif files reported by Gualtieri and Venturelli[11] for hematite at 300 and 1050 K. These clusters were truncated at all irons within 18.5 Å of the center and all coordinating oxygens for the room temperature structure, giving a total of 3044 atoms. The total radius of the truncated cluster was 19.0 Å, while the expanded lattice at 1050 K had a cluster radius of 20.4 Å. In Fig. S8g, the spectrum shown is the difference of the XANES spectra of the two clusters calculated at a temperature of 300 K, while in Fig. S8h, 0.4 eV of instrumental broadening was added and the expanded lattice was calculated at 1500 K. The expanded lattice with thermal disorder shows the best agreement with the experiment of all the models explored and is also plotted in Fig. 7.

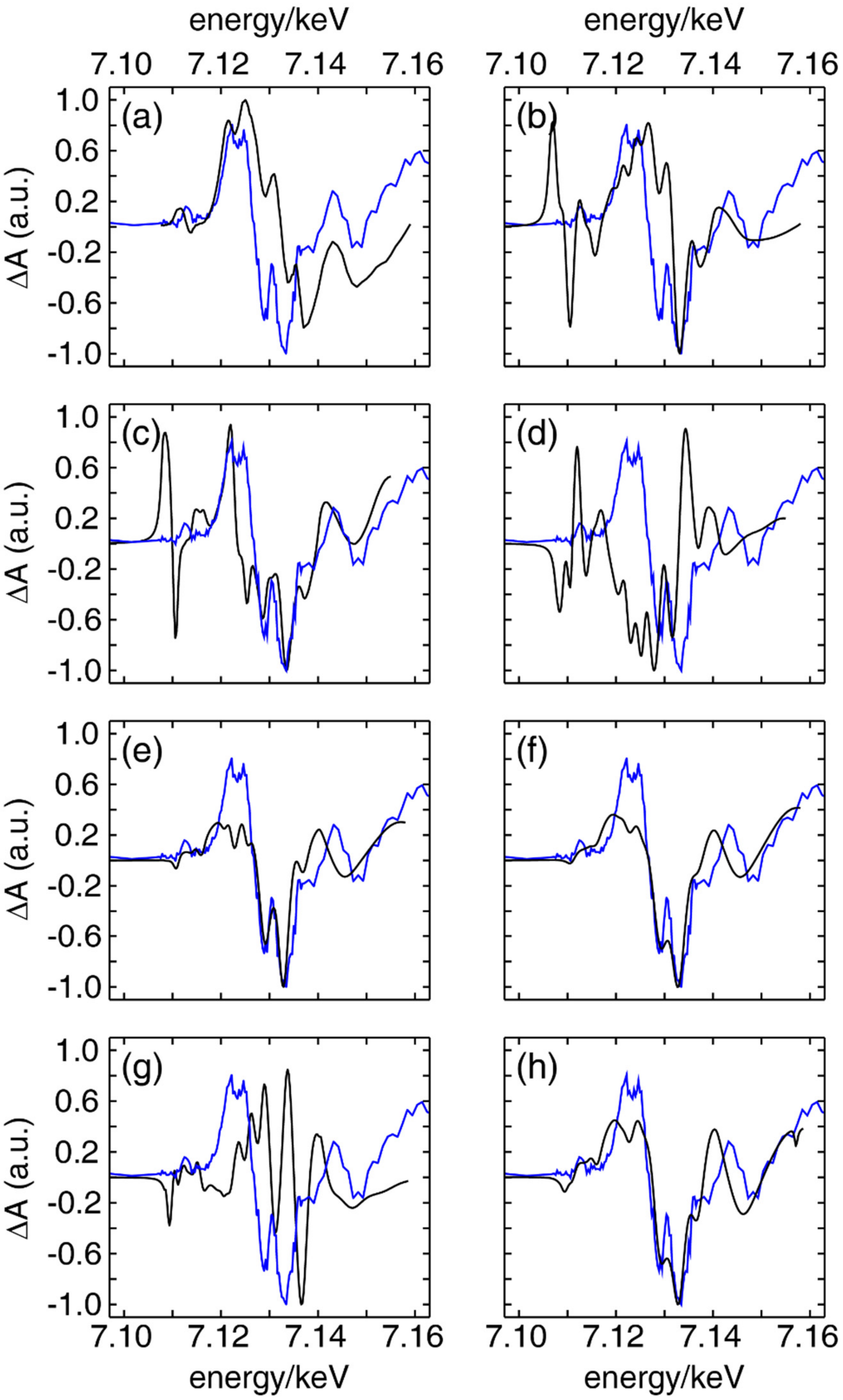

Fig. S8. The iron K-edge transient absorption spectrum measured at a delay time of 100 ps with a pump wavelength of 351 nm is shown in blue in all panels. The black spectra correspond to various models of an electronically excited and/or distorted lattice. Panels b-h were obtained from full multiple scattering calculations. (a) Experimental spectrum shifted by -1.4 eV, (b) calculated spectrum shifted by -1.4 eV, (c) electron small polaron distortion, (d) electron small polaron with spectrum of center iron shifted by -1.4 eV, (e) Debye-Waller broadening calculated at 1000 K, (f) broadening calculated at 1000 K with 0.6 eV instrumental broadening added, (g) thermal lattice expansion, (h) thermal lattice expansion with broadening calculated at 1000 K.

11. Nanosecond to microsecond transient absorption

Optical transient absorption spectroscopy on the ns-µs timescale was performed using a home-built apparatus. A tunable narrow band laser (Ekspla PL2210 Nd:YAG and OPO with a pulse duration of 50 ps) was used as the pump excitation and also served as the master 1kHz clock. A broadband super continuum fiber laser (Leukos STM with a pulse duration of 700 ps) was used as the probe. Time delays were achieved using a delay generator (SRS DG535) externally synchronized to the 1 kHz clock from the pump laser. The pump excitation was modulated at 500 Hz by an optical chopper (Newport model 3502). The transmitted probe intensity was spectrally resolved via a spectrometer (Acton Research Corporation Spectra Pro 2150i) and recorded with a line scan camera (Teledyne Dalsa Spyder3 1k). The instrument was controlled using home-written LabVIEW code.

12. IPCE calculation

The maximum theoretical IPCE spectrum for a photocatalytic model in which LMCT transitions have 100% quantum efficiency and d-d transitions have 0% quantum efficiency was calculated from the fit shown in Fig. 1 and the raw absorption and reflectance spectra shown in Fig. S1 according to Equation S3.

$$IPCE(\lambda) = (1 - 10^{A_1(\lambda)+A_2(\lambda)})\frac{R(\lambda)}{E(\lambda)} \tag{S7}$$

In this expression, the $A_n(\lambda)$ terms are the absorption spectra of the two LMCT bands shown in gray in Fig. 1 expressed in units of optical density. The parameters describing these two Gaussian bands are given in Table S1. $R(\lambda)$ corresponds to the reflectance spectrum and $E(\lambda)$ corresponds to the raw absorption spectrum (not reflectance corrected) shown in Fig. S1 in red and blue, respectively. The term in parentheses calculates the total percentage of photons absorbed only by the LMCT bands as a function of wavelength, while the multiplicative factor calculates the percentage of photons that are not reflected by the film and thus can be absorbed.

13. Other supporting figures

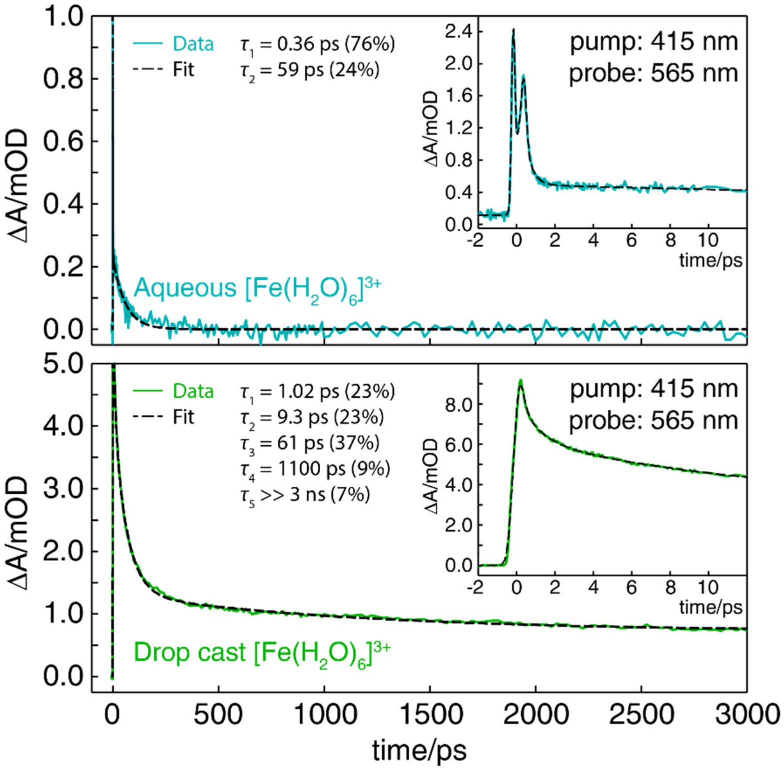

Fig. S9. (Top) Kinetic trace (cyan) taken from the OTA spectrum of aqueous $[Fe(H_2O)_6]^{3+}$ (OD 0.55 at 415 nm) following excitation at 415 nm, averaged over probe wavelengths from 560 to 570 nm. The trace was fit (dashed black) to the sum of two exponential decays (τ_1, τ_2) and a constant offset (τ_3 >> 3 ns), all convolved with a Gaussian IRF, plus a coherent artifact comprised of two Gaussians. The strong double-peaked coherent artifact (see inset) was also observed in a solvent blank (water). The fit gave an amplitude of zero for the τ_3 term and a lifetime of 0.36 ps for the τ_3 term, meaning the kinetics beyond the first picosecond are fully described by a single exponential with a time constant of 59 ps. (Bottom) Kinetic trace (green) taken from the OTA spectrum of a drop cast film of $[Fe(H_2O)_6]^{3+}$ on fused quartz following excitation at 415 nm, averaged over probe wavelengths from 560 to 570 nm. The trace was fit (dashed black) to the sum of four exponential decays (τ_1-τ_4) and a constant offset (τ_5 >> 3 ns) plus a coherent artifact, all convolved with a Gaussian IRF. Unlike the aqueous sample, the film shows a complex multiexponential decay consistent with a lattice heating model of the transient absorption and comparable to that observed in a hematite thin film (see Figs. 8 and S15).

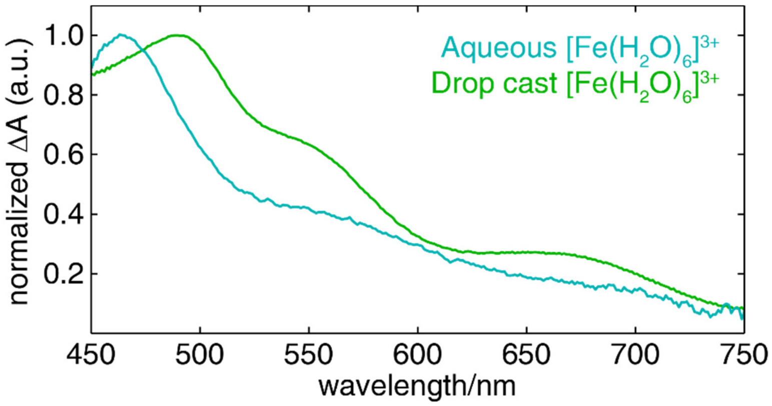

Fig. S10. Transient absorption spectra of aqueous (cyan) and drop cast (green) $[Fe(H_2O)_6]^{3+}$ samples following excitation at 415 nm averaged over all delay times between 20 and 25 ps in 0.5 ps steps. The spectra are normalized to their respective maxima.

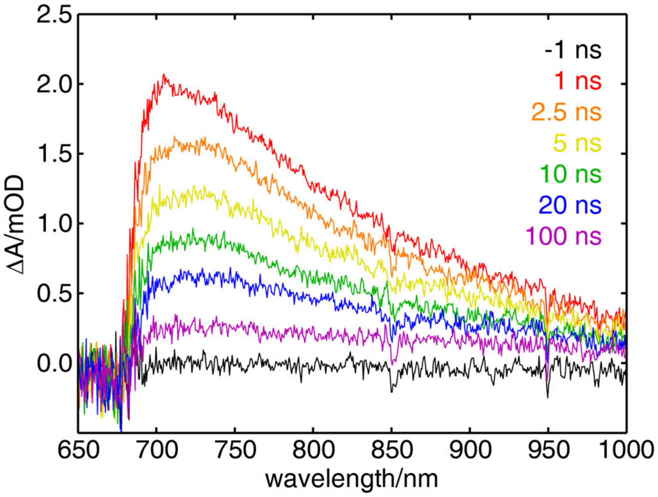

Fig. S11. The long-time NIR transient absorption spectra of a hematite thin film following excitation at 425 nm obtained with a white light probe spanning from 700 to 1000 nm. This probe spectrum is continuous across the 730-930 nm gap between those of the visible and NIR white light probes used in the ultrafast experiments shown in Figures 2 and S3. The TA spectra plotted here show no structure in this region, demonstrating that the NIR transient observed at times beyond 1 ns is the tail of the main ESA feature observed in the visible region at 580 nm.

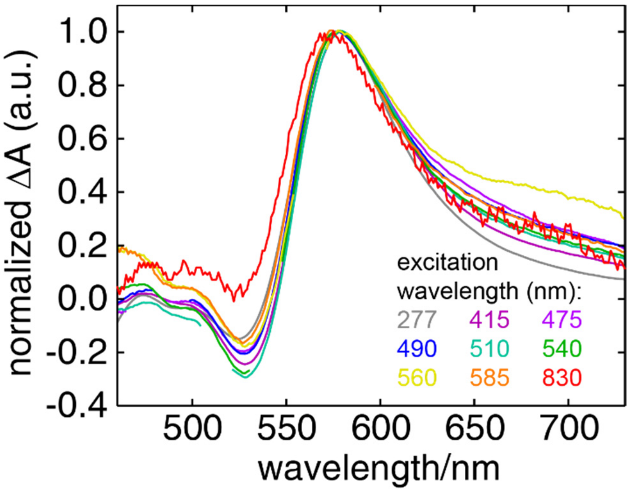

Fig. S12. OTA spectra of a hematite thin film 250 ps following excitation at a number of different wavelengths normalized to their respective maxima. All spectra qualitatively show the same features, demonstrating that the OTA at this delay time is independent of excitation wavelength. Due to the extremely low optical density beyond 600 nm, the 830 nm pump spectrum was obtained using a pump pulse energy of 10 μJ (38 mJ/cm^2 fluence).

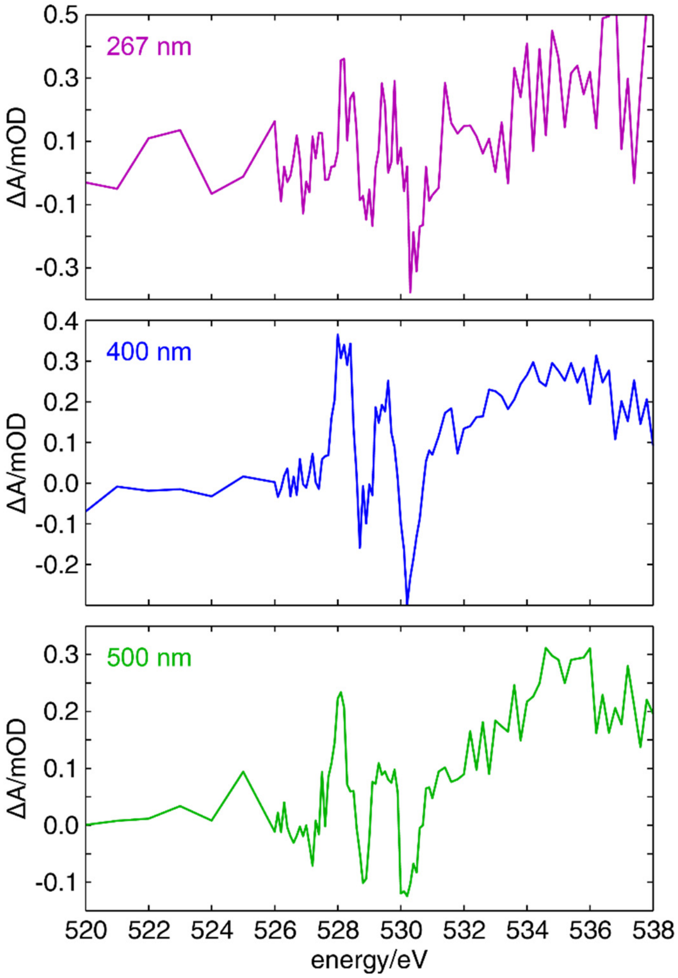

Fig. S13. Oxygen pre-edge XTA spectra of a hematite thin film 200 ps following excitation at three different wavelengths. All spectra qualitatively show the same features, demonstrating that the oxygen XTA at this time delay is independent of excitation wavelength.

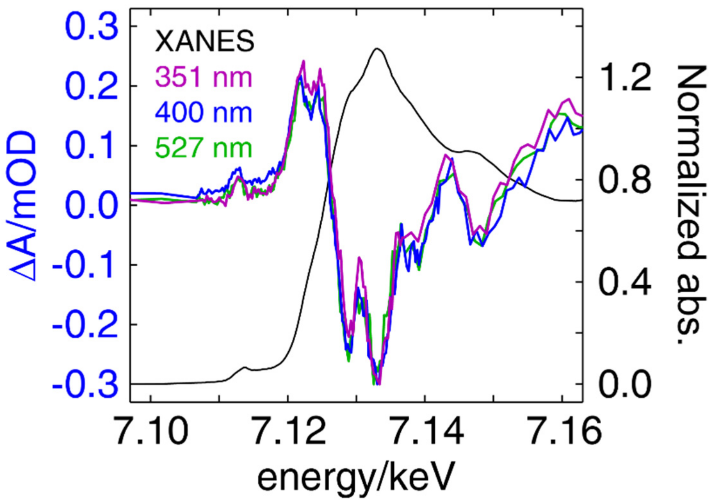

Fig. S14. Iron K-edge XTA spectra of a hematite thin film 100 ps following excitation at three different wavelengths normalized to their respective extrema. All spectra qualitatively show the same features, demonstrating that the iron K-edge XTA at this time delay is independent of excitation wavelength.

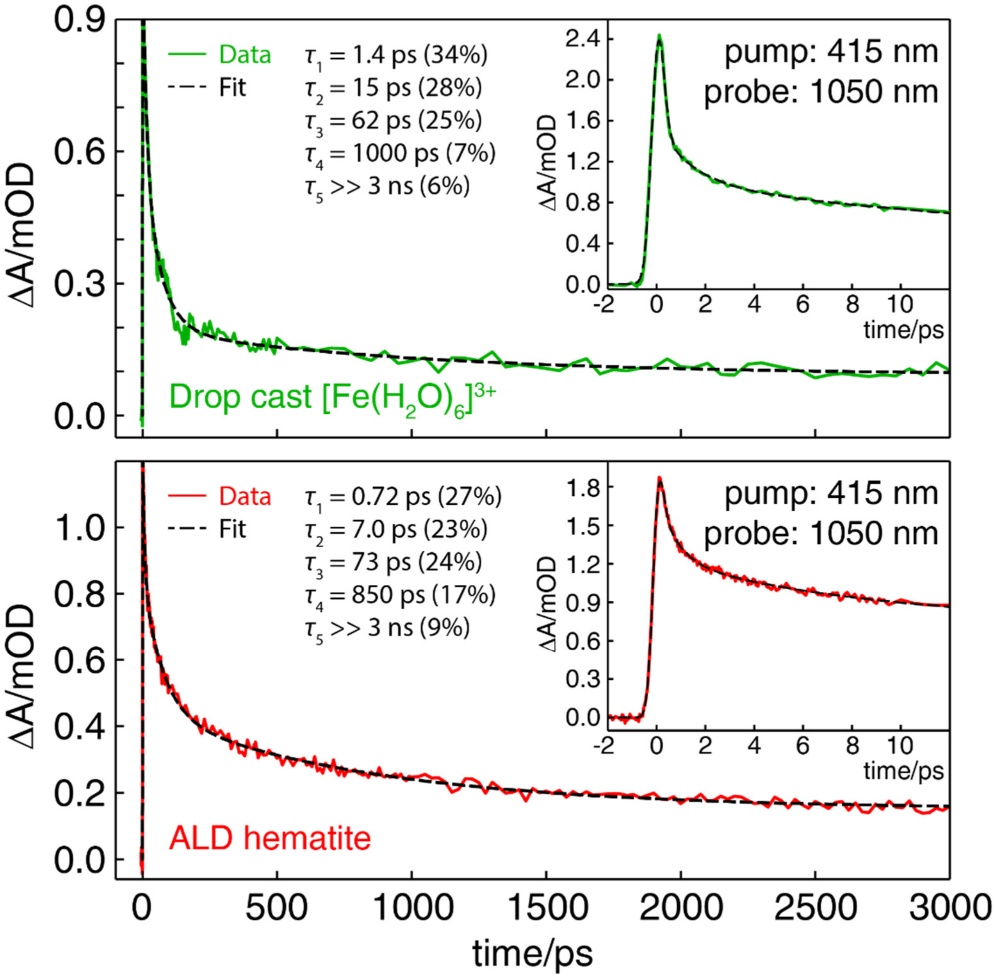

Fig. S15. Kinetic traces taken from the NIR transient absorption spectra of a drop cast film of $[Fe(H_2O)_6]^{3+}$ on fused quartz (top, green) and a hematite thin film grown by ALD on fused quartz (bottom, red) following excitation at 415 nm. The region (950-1150 nm) that was averaged to give the traces is shown in Fig. 2, with the average probe wavelength given above. The traces were each fit (dashed black) to the sum of four exponential decays (τ_1-τ_4) and a constant offset (τ_5 >> 3 ns) plus a Gaussian coherent artifact, all convolved with a Gaussian IRF. The time constants and percentages of the fit components are also shown. Both films show a complex multiexponential decay consistent with a lattice heating model of the transient absorption.

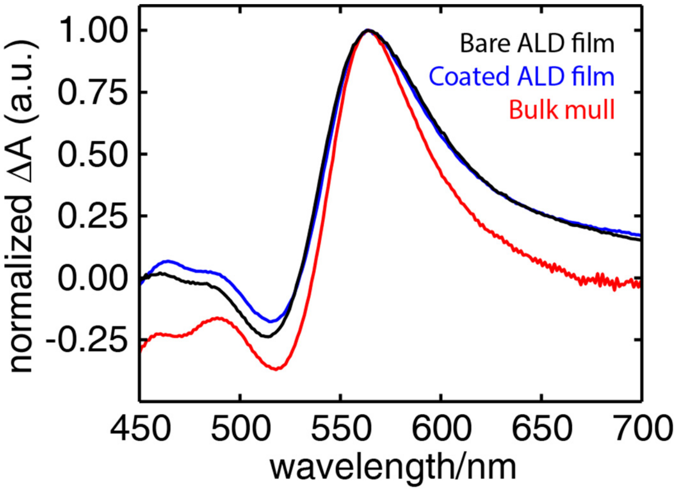

Fig. S16. OTA spectra of three different samples of hematite 200 ps following excitation at 415 nm normalized to their respective maxima. All spectra qualitatively show the same features, demonstrating that the OTA is not dominated by surface defects.

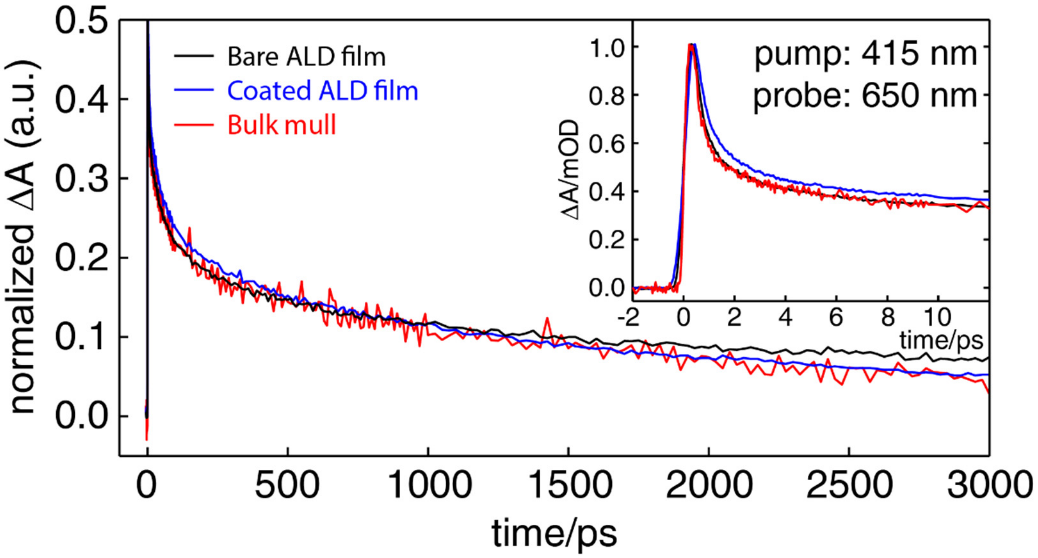

Fig. S17. Kinetic traces taken at a probe wavelength of 650 nm from the OTA spectra of three different samples of hematite following excitation at 415 nm. This probe wavelength was chosen because it corresponds to the feature assigned to free carrier absorption. The decays observed for the different samples show excellent agreement, demonstrating that the OTA is not dominated by surface defects.

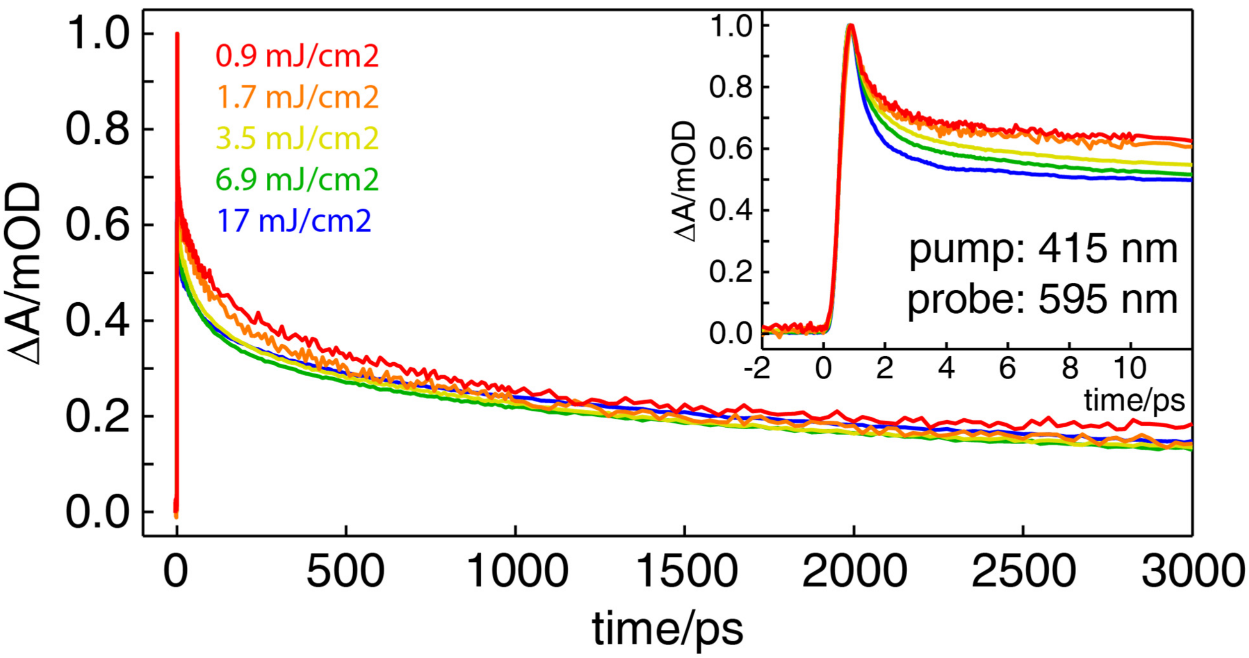

Fig. S18. Kinetic traces taken at a probe wavelength of 595 nm from the OTA spectra of a hematite thin film following excitation at 415 nm at several excitation fluences. The traces show that the decay kinetics are largely independent of fluence in the regime investigated here. We note that the sub-ps signal shows a stronger coherent artifact at higher excitation fluences due to the nonresonant response of the fused quartz substrate.

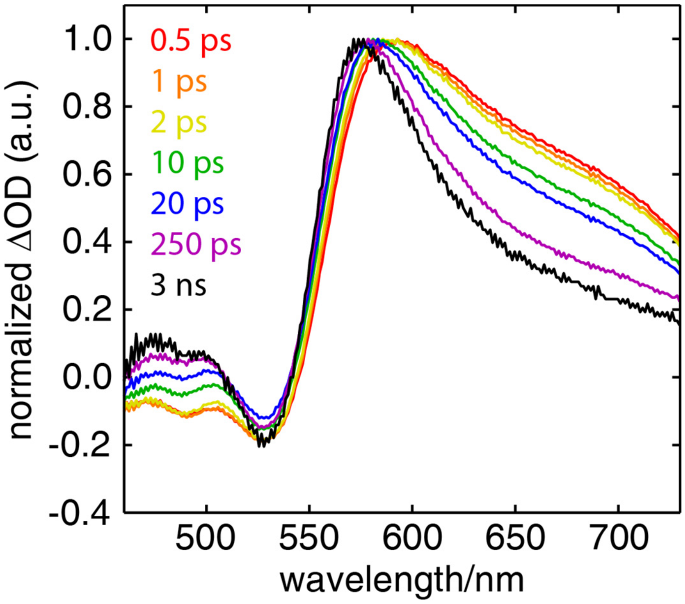

Fig. S19. A series of OTA spectra of a hematite thin film following excitation at 415 nm at a fluence of 3.5 mJ/cm^2 normalized to their respective maxima to highlight the evolution of the spectral shape. A broad ESA band at ~675 nm appears at early times but decays within 100 ps, and subsequent spectra do not show significant further changes. The same trends are observed here as in Fig. 9 of the main text, where the fluence was 17 mJ/cm^2, demonstrating that the early time (< 100 ps) decay kinetics are independent of fluence in the regime investigated here.

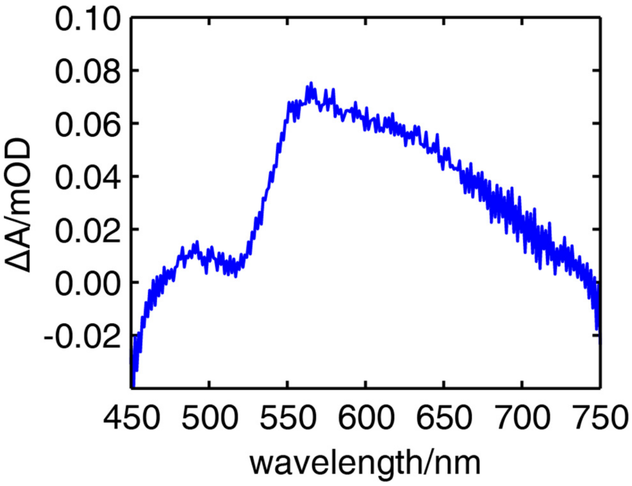

Fig. S20. Optical transient absorption spectrum at 20 ps following excitation at 415 nm with a pump fluence of 0.25 mJ/cm^2. Even at vanishingly low fluences, the OTA spectrum retains all the features of the thermal difference spectrum, demonstrating that thermal contributions dominate at any arbitrary excitation density. The approximate excited state population at this fluence is less than 0.1%.

14. References

1 A. B. F. Martinson, M. J. DeVries, J. A. Libera, S. T. Christensen, J. T. Hupp, M. J. Pellin and J. W. Elam, *J. Phys. Chem. C*, 2011, **115**, 4333–4339.

2 B. Klahr, S. Gimenez, F. Fabregat-Santiago, T. Hamann and J. Bisquert, *J. Am. Chem. Soc.*, 2012, **134**, 4294–4302.

3 S. R. Greenfield and M. R. Wasielewski, *Appl. Opt.*, 1995, **34**, 2688–2691.

4 W. M. Haynes and D. R. Lide, *CRC handbook of chemistry and physics : a ready-reference book of chemical and physical data*, CRC Press, Boca Raton, Fla., 2011.

5 M. W. Chase, *NIST-JANAF Thermochemical Tables*, American Chemical Society, Washington, D.C., 1998.

6 M. J. Frisch *et al*., *Gaussian 09, Revision A.02*, Gaussian, Inc., Wallingford CT, 2009.

7 A. D. Becke, *Phys. Rev. A*, 1988, **38**, 3098–3100.

8 C. Lee, W. Yang and R. G. Parr, *Phys. Rev. B*, 1988, **37**, 785–789.

9 A. Schäfer, C. Huber and R. Ahlrichs, *J. Chem. Phys.*, 1994, **100**, 5829–5835.

10 L. W. Finger and R. M. Hazen, *J. Appl. Phys.*, 1980, **51**, 5362–5367.

11 A. F. Gualtieri and P. Venturelli, *Am. Mineral.*, 1999, **84**, 895–904.

12 P. A. Heimann, T. E. Glover, D. Plate, H. J. Lee, V. C. Brown, H. A. Padmore and R. W. Schoenlein, in *AIP Conference Proceedings*, AIP Publishing, 2007, vol. 879, pp. 1195–1197.

13 N. Huse, T. K. Kim, L. Jamula, J. K. McCusker, F. M. F. de Groot and R. W. Schoenlein, *J. Am. Chem. Soc.*, 2010, **132**, 6809–6816.

14 G. Jennings, W. J. H. Jäger and L. X. Chen, *Rev. Sci. Instrum.*, 2002, **73**, 362–368.

15 X. Zhang, G. Smolentsev, J. Guo, K. Attenkofer, C. Kurtz, G. Jennings, J. V. Lockard, A. B. Stickrath and L. X. Chen, *J. Phys. Chem. Lett.*, 2011, **2**, 628–632.

16 L. X. Chen and X. Zhang, *J. Phys. Chem. Lett.*, 2013, **4**, 4000–4013.

17 J. J. Rehr, J. J. Kas, M. P. Prange, A. P. Sorini, Y. Takimoto and F. Vila, *Comptes Rendus Phys.*, 2009, **10**, 548–559.

18 J. J. Rehr, J. J. Kas, F. D. Vila, M. P. Prange and K. Jorissen, *Phys. Chem. Chem. Phys.*, 2010, **12**, 5503–5513.

19 J. E. Katz, X. Zhang, K. Attenkofer, K. W. Chapman, C. Frandsen, P. Zarzycki, K. M. Rosso, R. W. Falcone, G. A. Waychunas and B. Gilbert, *Science*, 2012, **337**, 1200–1203.

20 B. Ravel, *J. Synchrotron Radiat.*, 2001, **8**, 314–316.

21 B. Ravel and M. Newville, *J. Synchrotron Radiat.*, 2005, **12**, 537–541.

22 J. Sólyom, *Fundamentals of the Physics of Solids: Volume 1: Structure and Dynamics*, Springer Science & Business Media, Berlin, 2007.

23 A. Sanson, A. Zaltron, N. Argiolas, C. Sada, M. Bazzan, W. G. Schmidt and S. Sanna, *Phys. Rev. B*, 2015, **91**, 94109.

24 N. Adelstein, J. B. Neaton, M. Asta and L. C. De Jonghe, *Phys. Rev. B*, 2014, **89**, 245115.